Supporting Information

Bias-free Si-Based Photocathode for Efficient Photoelectrochemical Ammonia Synthesis and HMF oxidation

Experimental section

Preparation of Si

First, prepare a silicon wafe rserve as suitable substrate. The surface of the substrate is then cleaned and pretreated to remove any impurities and create a suitable texture for improved light absorption. Next, a thin layer of transparent conductive oxide (TCO) is deposited on the substrate. After that, a thin layer of intrinsic amorphous silicon (a-Si:H) is deposited on top of the TCO layer. Following this, a thin layer of amorphous silicon doped with hydrogen (a-Si:H) is deposited, serving as the p-type layer. This layer is followed by another layer of amorphous silicon doped with boron (a-Si: B), which acts as the n-type layer. Together, these two layers form the heterojunction (HJT) structure. The final step involves depositing a metal contact layer on top of the n-type layer. This layer made of silver, serves as the back electrode and completes the circuit.

Preparation of TiO_2

Thin layers of amorphous TiO_2 were deposited onto the Si photocathode using a thermal ALD system (Ensure NanoTech, China). TiO_2 layers were deposited at a reaction chamber temperature of 150 ℃ using tetra (dimethylamino) titanium (TDMAT) (99.99 %, Aldrich) and high-purity H_2O as the Ti and O precursors, respectively. TiO_2 layers were deposited in pulse mode under a nitrogen flow of 5 sccm and the growth rate was ~0.056 nm per cycle at 150 ℃. The thickness of the TiO_2 film can be regulated by controlling the cycle number. The number of ALD cycles was 185,370 and 555, and a film thickness of ~10 nm, 20 nm and 30 nm.

Preparation of TiO_2 without O_v

P25 (TiO_2 powder) is dispersed in water/iso-propanol (3 mg/ml, volume ratio of water: isopropanol=3:7) with 30 min sonication to make a good suspension. After that, it is spin-coated on Si at 2000 rpm for 20s to obtain Si-TiO_2 without O_v.

Preparation of NiCuO

Nickel foam (NF) was used as the substrate. NF was sonicated in 1 M HCl solution for 10 min to remove the oxide layer on the surface of NF, then sonicated in ethanol for 5 min, rinsed with deionized water, and finally dried in air. The co-electrodeposition was carried out in a standard three-electrode electrochemical cell, in which NF was used as the working electrode, the parallelly placed platinum sheet was used as the counter electrode, and Ag/AgCl (3 M KCl) was used as the reference electrode. The electrolyte consisted of 6 mmol $Ni(NO_3)\times 6H_2O$ and 6 mmol $Cu(NO_3)\times 3H_2O$ dissolved in 100 mL deionized water. Then, potentiostatic electrodeposition was carried out at -1.0 V (relative to Ag/AgCl) and 25 °C. The deposition time of Ni Cu-OH is 300 s. After deposition, rinse with deionized water and ethanol. After drying, it was placed at 60 °C for 6 h, and then placed at 300 °C for 3 h, so that it was successfully oxidized to NiCuO.

Material characterizations

X-ray diffraction (XRD) was used to study the phase structure using Cu Kα radiation (λ = 1.54 Å) at a working potential of 45 kV and a current of 40 mA (Philips X'pert MPDE mpyrean). The morphology and elemental

distribution of the Si-TiO_2 was analyzed by Bruker D8 field emission scanning electron microscope (SEM) equipped with an energy dispersive X-ray spectroscopy (EDS) system. The electron paramagnetic resonance (EPR) spectra was characterized by Bruker A300. The EPR spectrum and sample are placed in the paramagnetic tube respectively, and then fixed on the EPR resonator. The test was performed at room temperature, and the paramagnetic tube was sealed with a plug and a sealing film.

photoelectrochemical measurement

Electrochemical results such as linear sweep voltammetry (LSV) curves, and electrochemical impedance spectroscopy (EIS) Nyquist plots under dark and illumination conditions were obtained with the CHI660E electrochemical workstation in a standard three-electrode configuration in an air-tight liquid flow pool. Specifically, the obtained Si-TiO2 photocathode was applied as the working electrode, Ag/AgCl as the reference electrode, and Pt as the counter electrode. The working electrode and counter electrode were separated by a Nafion 211 membrane. For PEC nitrate reduction test, the electrolyte was 0.1 M KNO_3 and 10 mM H_2SO_4, the chronoamperometry method is used for 1 h with different applied potentials when testing PEC nitrate reduction. For 5-hydroxymethyl furfural oxidation test, the electrolyte was 50 mM 5-hydroxymethyl furfural and 1 M KOH. For glycerol oxidation test, the electrolyte was 0.1 M glycerol and 1 M KOH. Solar simulator was used as the light source, which was calibrated to AM 1.5 G (100 mW/cm^2). The potentials were measured versus (vs.) the Ag/AgCl reference electrode, which can be converted into the reversible hydrogen electrode (RHE) scale by the Nernst equation:

E (vs. RHE) = E (vs. Ag/AgCl) +$E_{Ag/AgCl}$ +0.059 V ×pH

($E_{Ag/AgCl}$ = 0.1976 V vs. RHE at 25 ℃)

In this equation, E (vs. RHE) refers to the converted potential vs. RHE and E (vs. Ag/AgCl) is the external potential measured against the Ag/AgCl reference electrode. The voltage when the photocurrent begins to increase linearly is called the onset potential.[1, 2]

Product analysis

After reaction, the possible gas product was checked using gas chromatography (GC-2010, Shimadzu) equipped with a flame ionization detector (FID) and thermal conductivity detector (TCD) by injecting gas sample from the cathode part. Ammonia was tested using the typical indophenol-blue method to determine NH_4^+ concentration.[3] The 500 μL resulting catholyte was collected into a vial and then mixed with the sequential addition following solution. (1) 400 μL of 1 M NaOH containing 5 wt% salicylic acid, 5 wt% sodium citrate, (2) 100 μL of 0.05 M NaClO and (3) 30 μL of 1 wt% sodium nitroferricyanide solution. This was then sonicated thoroughly and kept in the dark at room temperature for 2 h. Afterwards, UV-vis absorption spectra of the resulting solution were recorded, with wavelength between 550 to 850 nm. By using the peak absorbance around 661 nm, the concentration of NH_4^+ can be calculated according to calibration results using the standard solution containing given NH_4^+ concentration (Figure S1).

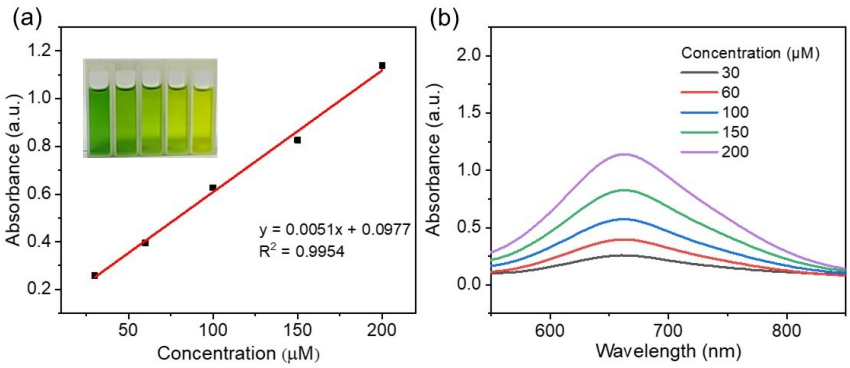

Figure S1: (a) linear fitting curve of the absorbance value at 661 nm and the concentration,(b) UV-vis spectra of standard NH_4^+ solution

Nitrite was detected using the Griess Reagent method. Typically, 50 µL of resulting catholyte was transferred into a vial and mixed with 50 µL of Griess Reagent and 900 µL of Milli-Q water. The mixture was incubated at room temperature in the dark for 30 min and the concentration on NO_2^- was determined by the UV-vis spectra of the solution. The peak absorbance around 525 nm was used to calculate the NO_2^- concentration according to the calibration curves obtained by testing solutions of $NaNO_2$ with known concentrations (Figure S2).

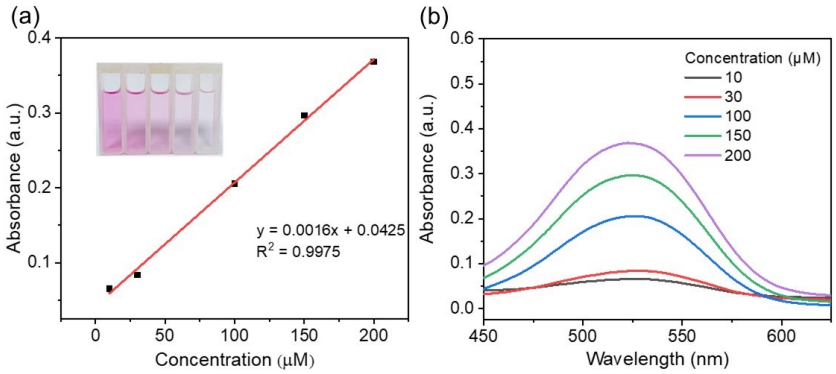

Figure S2: (a) linear fitting curve of the absorbance value at 525 nm and the concentration, (b) UV-vis spectra of standard NO_2^- solution

The possible gas product was injected into a gas chromatograph (GC-2010, Shimadzu) equipped with a flame ionization detector (FID) and a thermal conductivity detector (TCD).

Faradaic efficiency and yield rate calculation

The faradaic efficiency (FE) of products from nitrate reduction was determined by the following equation:

$$FE = \frac{n \times F \times C \times V}{Q} \times 100\%$$

Where n is the number of the electrons required for the formation of desired product from nitrate reduction (n=8 for NH_4^+, n=2 for nitrite); F is the Faraday constant (F = 96485.33), C is the detected product molar concentration from UV-vis method, V is the catholyte volume, and Q is the total charge recorded throughout the test. The

production yield rate (μmol/h•cm^2) is calculated from the equation:

$$Yield\ rate = \frac{C \times V}{t \times A}$$

Where C (μM) is the detected product molar concentration, V is the catholyte volume, t is the reaction time (h), and A (cm^2) is the surface area of the photocathode.

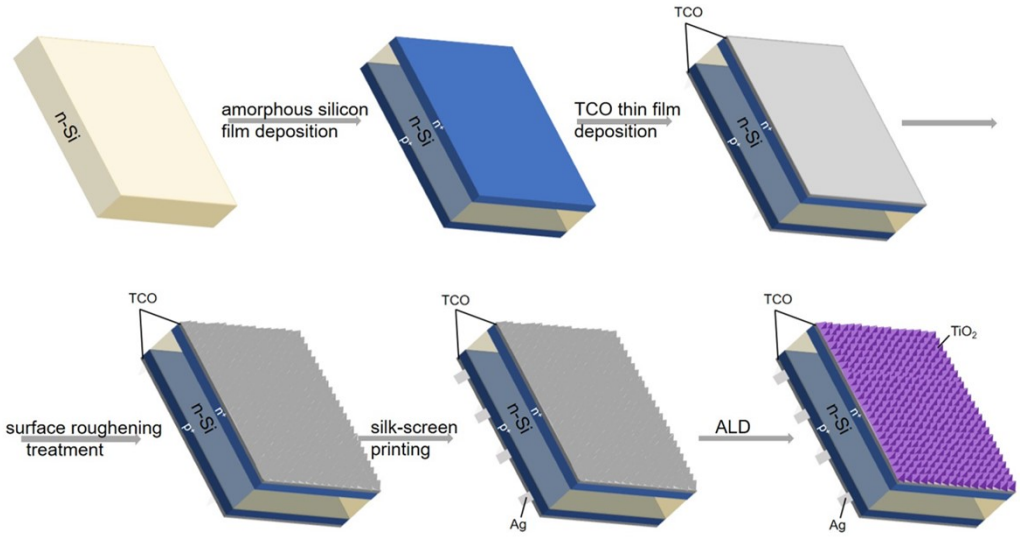

Figure S3: Schematic diagram of step-by-step fabrication process of the TiO_2/Si photocathode.

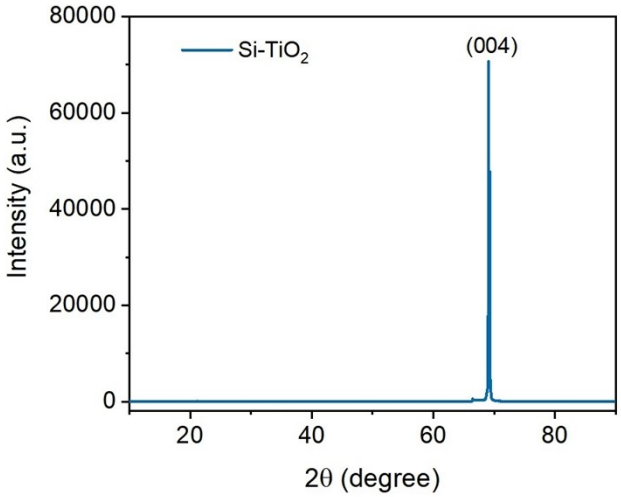

Figure S4: XRD patterns of Si-TiO_2.

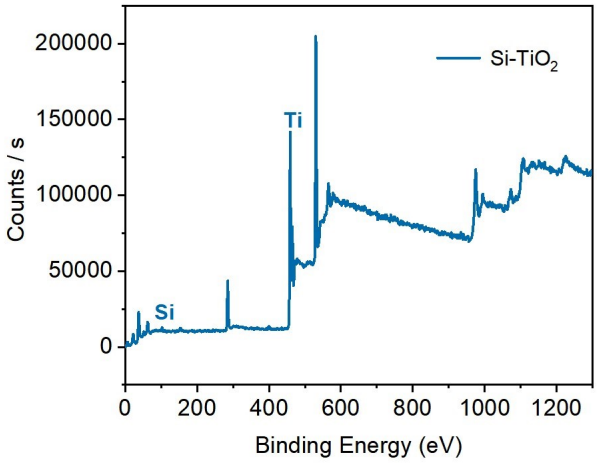

Figure S5: XPS patterns of Si-TiO_2.

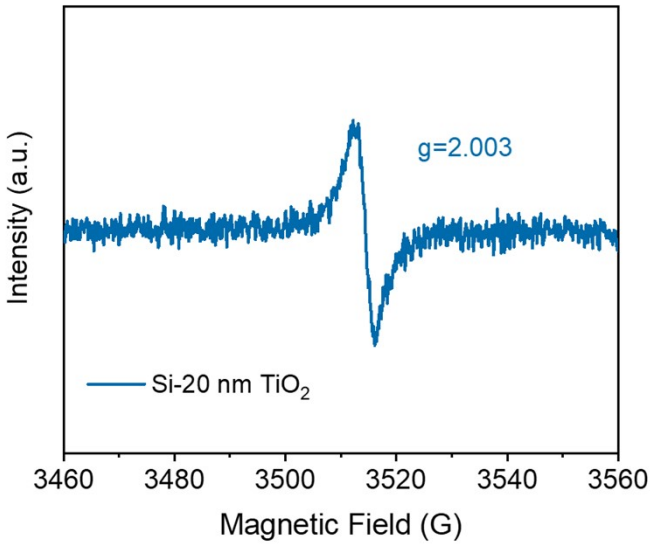

Figure S6: EPR spectra of Si-20 nm TiO_2 photocathode.

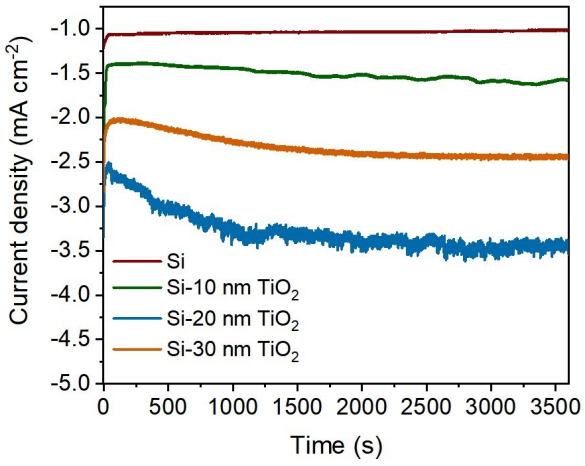

Figure S7: 1 hour stability of different TiO_2 thickness of Si photocathode in 0 V vs. RHE.

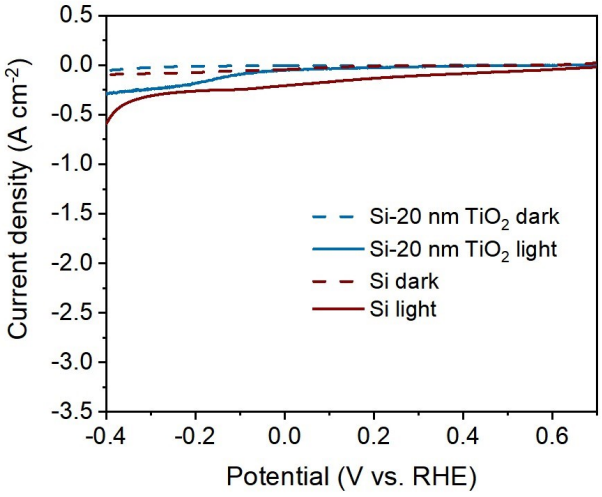

Figure S8: Linear sweep voltammetry curves of Si-20 nm TiO_2 and Si photocathode in 0.1 M K_2SO_4.

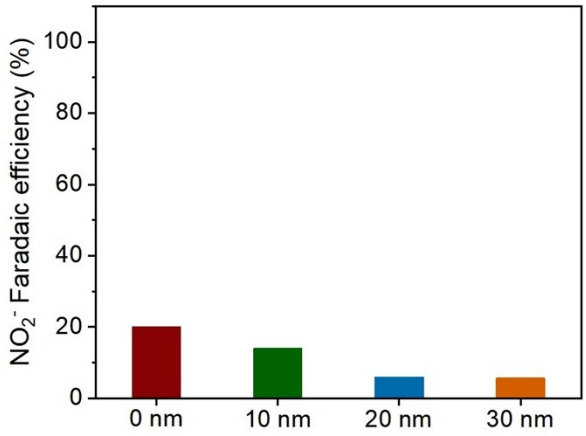

Figure S9: NO_2^- Faradaic efficiency of different TiO_2 thickness Si-TiO_2 in 0 V vs. RHE.

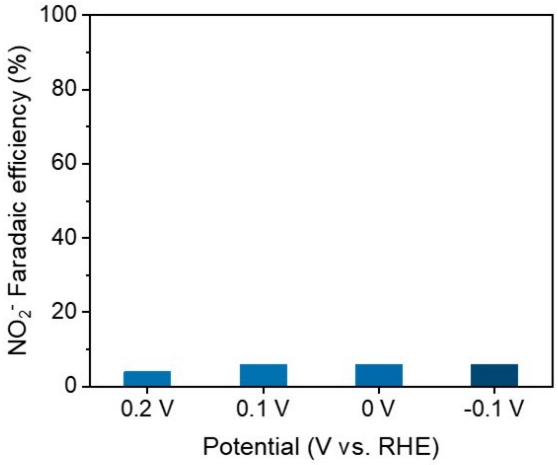

Figure S10: NO_2^- Faradaic efficiency of Si-TiO_2 in different applied potentials.

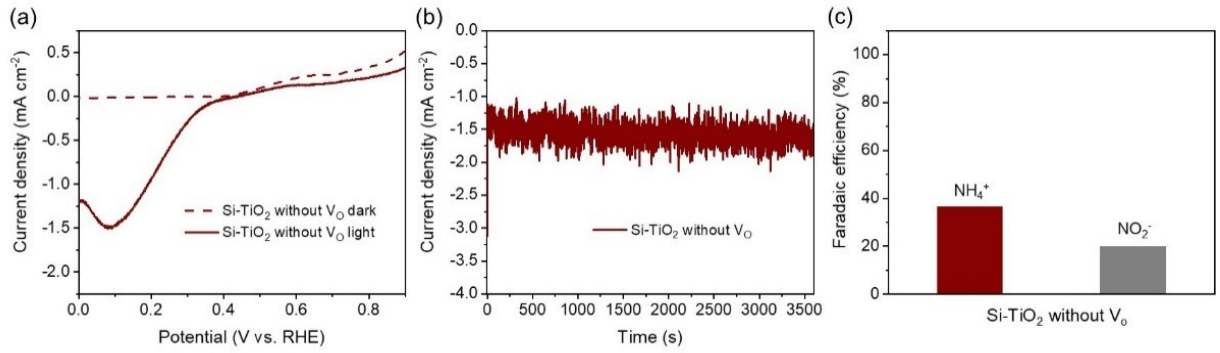

Figure S11. a) LSV curves b) 1 hour stability and c) Faradaic efficiency of TiO_2 without O_v in 0 V vs. RHE.

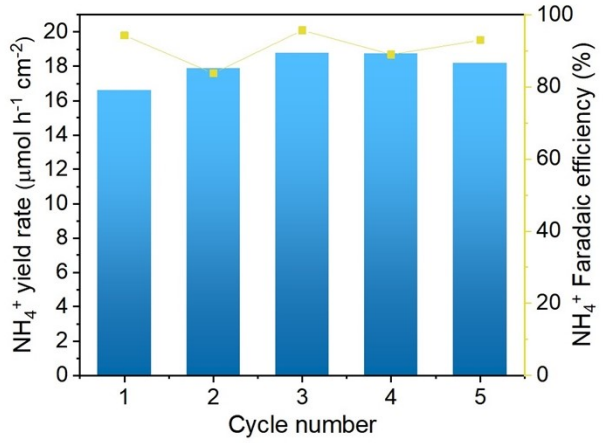

Figure S12: Continuous cycle stability test of Si-20 nm TiO_2 photocathode in 0 V vs. RHE.

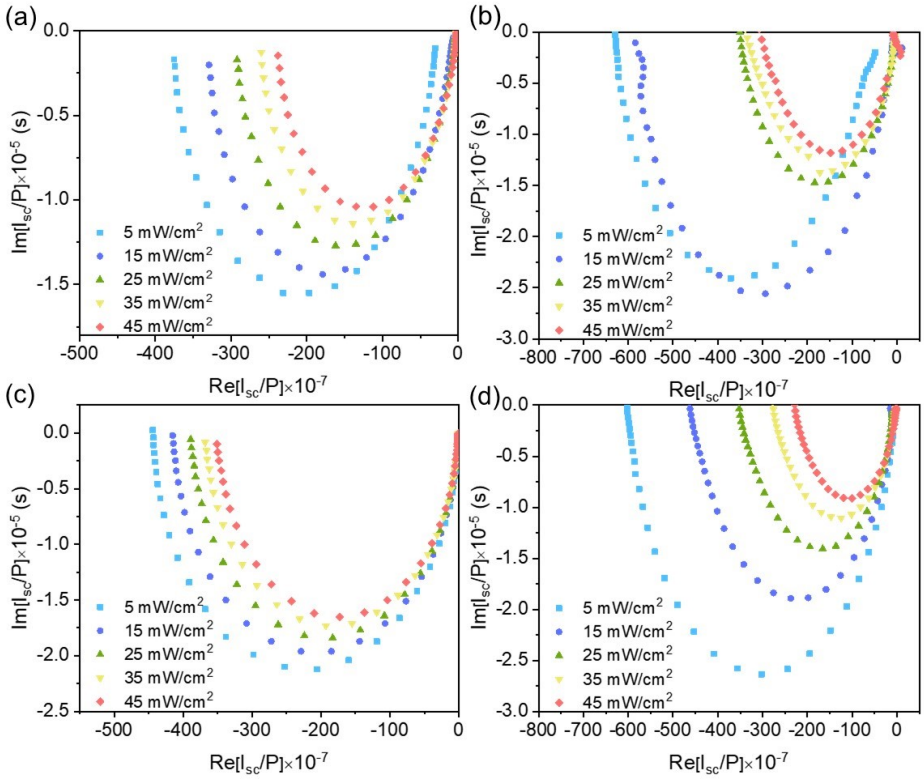

Figure S13: IMPS spectra of the a) Si, b) Si-10 nm TiO_2, c) Si-20 nm TiO_2, d) Si-30 nm TiO_2 photocathode at 590 nm.

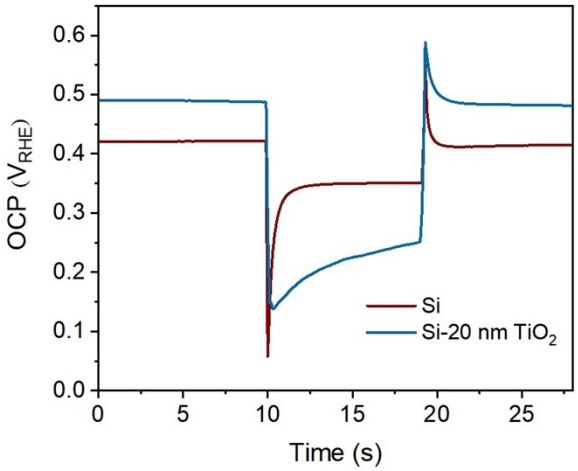

Figure S14: Open circuit potentials of Si-20 nm TiO_2 and Si photocathode.

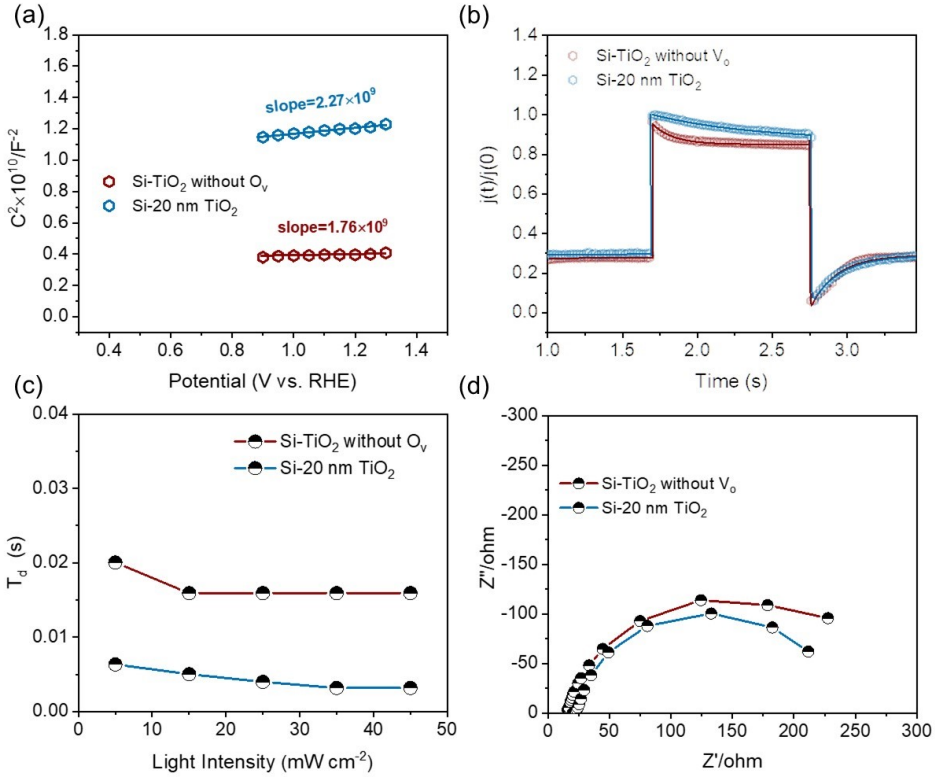

Figure S15: a) Mott-Schottky b) transit photocurrent spectra c) transfer time of photogenerated carriers generated and c) Nyquist plots of the Si-20 nm TiO_2 and Si-TiO_2 without V_o.

First, as shown in Figure S15 (a), the slope of the linear part of Si-20 nm TiO_2 is the largest (2.27×10^9), which is higher than that of the Si-TiO_2 photocathode without hypoxia. This means that the interface charge density of the Si-20 nm TiO_2 electrode is low, that is, when oxygen vacancies exist, obvious charge extraction will be induced at the interface between the TiO_2 catalyst and the electrolyte.

Secondly, Figure S15 (b) shows the transient photocurrent decay of the photocathode. We found that the Si-20 nm TiO_2 photocathode has a smaller photocurrent spike and a wider saturated photocurrent region than the Si-TiO_2 without Vo photocathode, which indicates less carrier recombination and effective photoelectron transfer in the electrode.

Then, in order to understand the surface/interface recombination or transfer of photogenerated carriers, IMPS measurements were performed, as shown in Figure S15 (c). It can be found that the photoinduced carrier transfer time of Si-20 nm TiO_2 photocathode is shorter than that of Si-TiO_2 without V_o photocathode, indicating that oxygen vacancies effectively improve the charge transfer efficiency.

As shown in Figure S15 (d), the charge transfer kinetic mechanism of Si-20 nm TiO_2 photocathode and Si-TiO_2 without Vo photocathode was further determined by electrochemical impedance spectroscopy (EIS) measurement. The R_1 and R_{ct} values of the si-20nm TiO_2 photocathode are smaller than those of the Si-TiO_2 without V_o photocathode. This means that oxygen vacancies effectively promote the transfer efficiency of carriers from the inside of the photocathode to the photocathode electrolyte interface, which means effective charge separation and transfer.

The results show that the Si-TiO_2 photocathode without oxygen vacancies is inferior to the Si-20 nm TiO_2 photocathode in the transfer of photogenerated carriers, transient photocurrent attenuation, surface/interface recombination or transfer of photogenerated carriers, charge separation and transfer. These results further illustrate the advantages of oxygen vacancy photovoltaic electrodes.

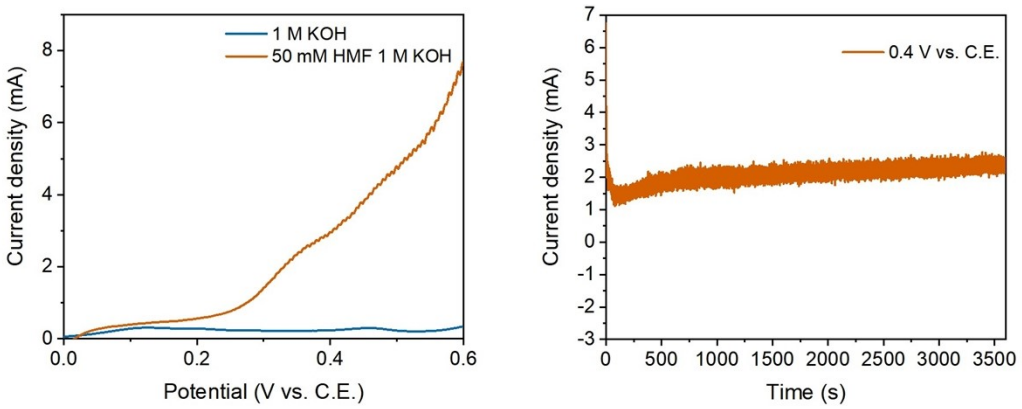

*Figure S16: (a) LSV for HMFOR and OER by Cu foam. (b) The HMFOR stability of 1h at 0.4 V (vs. C.E.). (Cu foam area is:2 cm*2 cm)*

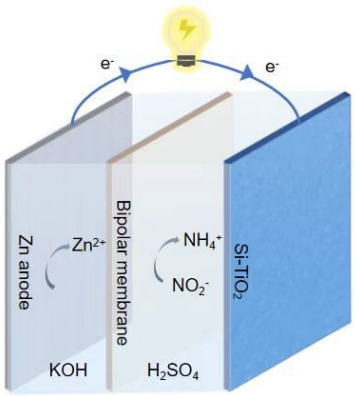

Figure S17: Schematic of the Zn-nitrate battery

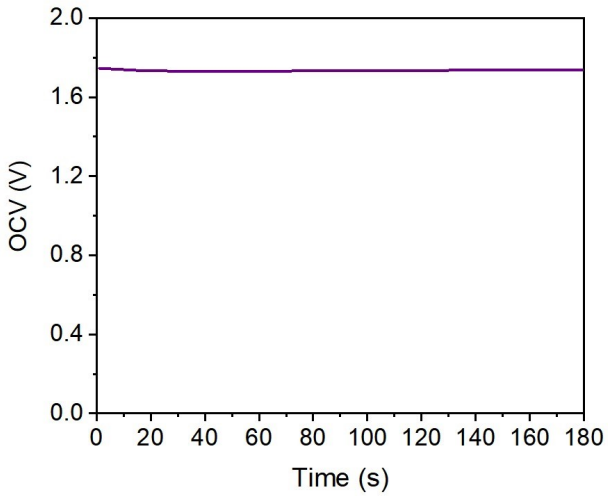

Figure S18: The OCV of Zn-NO_3^- fuel cell.

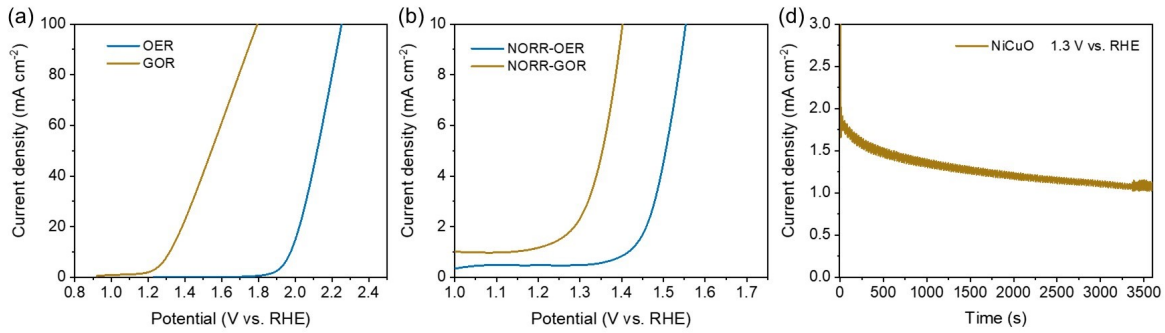

Figure S19: (a) LSV for GOR by NiCuO and OER by Pt. (b) Comparison of LSV for NO_xRR-OER and NO_xRR-GOR for full cell studies. (c) The NO_xRR-GOR stability of 1 h at 1.3 V vs. RHE.

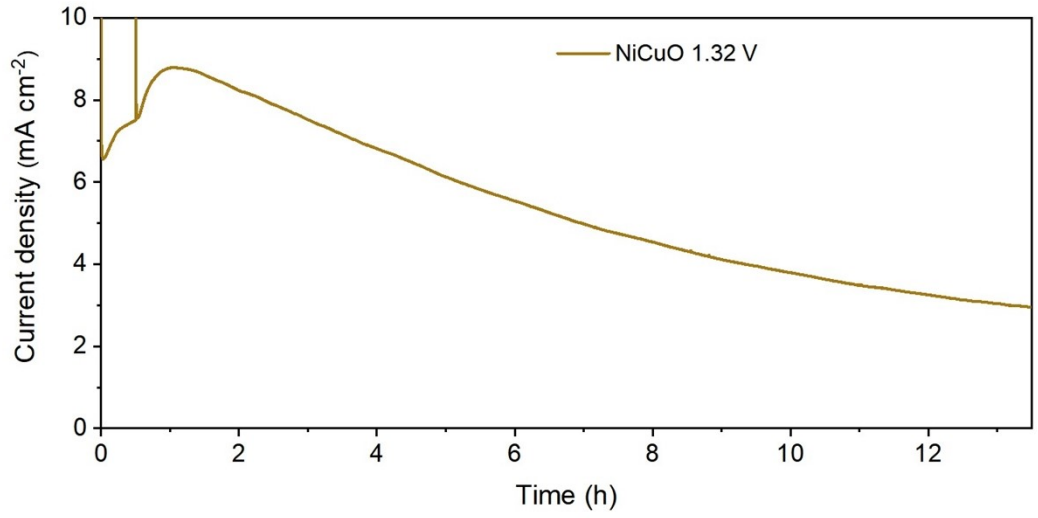

Figure S20: Stability test of NiCuO in 1.32 V vs. RHE.

Reference

1. L. Xia, F. Weiqiang, B. Yajie, L. Ying, W. Fengfeng, B. Hongye and S. Weidong, *Chemical Engineering Journal*, 2022, **433**, 133225.
2. L. Lintao, F. Kuang, H. Dingwang, W. Kang, L. Yuan, G. Zhiyou, N. Yun Hau and J. Feng, *Chemical Engineering Journal*, 2020, **396**, 125264.
3. R. Daiyan, T. Tran-Phu, P. Kumar, K. Iputera, Z. Tong, J. Leverett, M. H. A. Khan, A. Asghar Esmailpour, A. Jalili, M. Lim, A. Tricoli, R.-S. Liu, X. Lu, E. Lovell and R. Amal, *Energy & Environmental Science*, 2021, **14**, 3588-3598.